PAPER

Differential pressure sensor using flexible piezoelectrics with pyroelectric compensation

IOP Publishing Smart Materials and Structures
Smart Mater. Struct. **30** (2021) 035020 (12pp) https://doi.org/10.1088/1361-665X/abdcfc

Differential pressure sensor using flexible piezoelectrics with pyroelectric compensation

Arun K Ramanathan, Leon M Headings and Marcelo J Dapino

NSF IUCRC on Smart Vehicle Concepts, Department of Mechanical and Aerospace Engineering, The Ohio State University, Columbus, OH, United States of America

E-mail: dapino.1@osu.edu

Received 22 October 2020
Accepted for publication 18 January 2021
Published 5 February 2021

Abstract

Polyvinylidene fluoride (PVDF) is a mechanically tough, low density piezoelectric polymer commercially available as a flexible film that can be conformed to arbitrarily-shaped surfaces using simple adhesive bonding. A fundamental challenge that prevents the implementation of piezoelectric sensors for pressure sensing applications is their inability to measure static or very low frequency signals. Further, due to their large pyroelectric constants, they are limited to measurements where the rate of change in temperature is smaller than the lower cutoff frequency of the system. Under steady flow conditions, the cantilever unimorph possesses the highest sensitivity compared to other conventional configurations such as compression, doubly clamped unimorphs, or diaphragms. However, to preserve the overall noninvasive nature and linearity of the sensor, it is necessary to optimize the geometry and material properties in order to maximize charge output while minimizing deflection. To address these challenges, this work focuses on the development of a cantilever PVDF unimorph for static differential pressure measurement with pyroelectric compensation. A design optimization procedure to maximize the charge sensitivity of a cantilever unimorph is presented and the optimized cantilever is interfaced with a large-time-constant, drift-compensated charge amplifier for near-static pressure measurements. Voltage error due to temperature changes accompanying the input flow is compensated using a compressive mode sensor and an empirical compensation algorithm. Within the investigated range, the sensitivity of the fabricated sensor is 1.05 mV Pa^{-1} with an average resolution of 10 Pa and 97.3% linearity.

Keywords: piezoelectric PVDF, static sensing, pyroelectric compensation, cantilever unimorph, compressive, wind tunnel measurements

1. Introduction

In the field of experimental aerodynamics, differential pressure sensors that can simultaneously exhibit high temporal and spatial resolution are required [1]. Automotive aerodynamic measurements typically require surface pressure sensors capable of static differential pressure measurements from −2 to 2 kPa with a response time of less than 10 ms [2]. Commercial piezoresistive pressure transducers utilized for wind tunnel measurements are rigid, exhibit poor resolution due to their low sensitivity, and often involve complex conditioning electronics [3]. Further, they require time consuming fixturing that renders the tested parts unusable after measurements [4, 5]. Capacitive pressure sensors [6, 7] are advantageous due to their low power requirement, non-invasiveness, and low temperature dependence. However, the relationship between the pressure applied to them and their change in capacitance is non-linear. Further, the high sensitivity requirement of aerodynamic measurements warrants a viscoelastic construction resulting in a slower response time and creep tendency. Relatively new measurement techniques such as pressure-sensitive paint (PSP) can provide high spatial resolution [8]. Disadvantages of PSP systems include a poor dynamic response, requirement of expensive visual recorders

and image processing systems, and degradation of sensitivity over time.

In this context, flexible piezoelectric polymers serve as a promising alternative to conventional aeroacoustic transducers. PVDF is a flexible, low-density polymer manufactured commercially as thin sheets with thicknesses ranging from 9 μm to 100 μm. PVDF is relatively low cost and the flexibility offered by the polymer facilitates simplified instrumentation for flow investigations. However, one of the fundamental drawbacks of piezoelectric sensors is their inability to hold the charge displaced due to applied pressures. Therefore, almost all of the pressure sensors developed with piezoelectrics are limited to flow detection and oscillatory flow measurements [9, 10]. Charge amplifiers are typically used to enable a voltage readout of the charge displaced by a piezoelectric sensor in response to an applied pressure. They are relatively simple in construction with a small footprint which enables integration of the signal conditioner within the sensor itself [11]. The voltage gain and time constant of the charge amplifier are primarily determined by its feedback capacitance and resistance. Increasing the time constant comes at the expense of a reduction in voltage gain and increased signal error due to voltage drift and pyroelectricity [12, 13]. Therefore, in order to measure static differential pressure with high resolution, the charge per unit of applied pressure, defined as the charge sensitivity of the sensor, should to maximized.

Piezoelectric sensors respond to applied pressure under compression (d_{33} mode) or bending (d_{31} mode). The application of PVDF sensors in compressive mode is limited to large, unsteady surface pressure measurements (on the order of several kilopascals) in wind tunnels [14, 15], marine applications [16], and impulse measurements [17]. Diaphragm-type sensors (bending mode) are also limited to only unsteady pressure measurements ($\geqslant$50 Hz) [18] and energy harvesting applications [19, 20]. Static pressure measurements using the above sensor configurations require a large sensor area to achieve high time constants. Under steady flow conditions, for a given sensor geometry, the charge sensitivity of an optimized cantilever unimorph is three orders of magnitude greater than a compressive (d_{33} mode) design and three times higher than a doubly clamped unimorph with an optimized electrode coverage [21]. Although cantilever configuration has been utilized in static differential pressure measurements using piezoresistive technology [22, 23], piezoelectric cantilever unimorphs have been utilized only for dynamic pressure measurements [24, 25]. Piezoelectric PVDF unimorphs have not been used for static differential pressure measurements.

Piezoelectric sensors operating in bending require a substrate in order to produce a non-zero charge output. The constitutive equations for a piezoelectric unimorph operating below its fundamental frequency suggest that there exist optimum thickness and elastic modulus ratios of the PVDF layer to the substrate for maximum charge sensitivity [26]. Charge generated by a piezoelectric sensor is proportional to its surface area. However, in order to preserve the low profile, fast response, and linear characteristics of PVDF for a targeted spatial resolution, the surface area and thickness of the pressure sensor must be limited.

Piezoelectric materials also exhibit pyroelectricity under non-isothermal conditions. The net charge output of a piezoelectric sensor is an algebraic sum of the charge generated due to the piezoelectric and pyroelectric effects [27]. The pyroelectric coefficient of PVDF is several orders of magnitude larger than its piezoelectric coefficients ($p = 30$–40 μC m^{-2} °C^{-1}). Therefore, its application is limited to measurements where the rate of change of temperature is much smaller than the lower cutoff frequency of the system [24, 28]. The change in temperature during a typical wind tunnel test could be up to 1 °C [29]. For the sensor presented in this work, that would generate charge corresponding to a pressure measurement of 0.5 kPa. Therefore, piezoelectric sensors for near-static pressure measurements under varying thermal conditions require compensation techniques to remove the pyroelectric component of the measured voltage. At present, the temperature compensation techniques for piezoelectrics can be divided into two categories: sensitivity compensation and pyroelectric compensation. Most temperature compensation schemes are based on sensitivity compensation, which involves simultaneous measurement of temperature using a thermocouple to compensate for the change in piezoelectric sensitivity [30, 31]. Pyroelectric compensation utilizes data-driven empirical pyroelectric models to develop compensation algorithms [13, 32]. A drawback of these techniques is their susceptibility to noise contamination of the compensated voltage due to the different measurement principles of the active sensor and the compensator, usually a thermocouple. The forementioned compensation schemes are only implemented for dynamic measurements. Compensation schemes suitable for long-time static pressure measurements are not available in the literature. Recently, we proposed a technique for compensating the pyroelectric noise with a piezoelectric PVDF sensor in compressive mode [33].

The objective of this work is to demonstrate a high-sensitivity, near-static differential pressure sensing system based on a cantilever PVDF unimorph with pyroelectric compensation. An analytical design framework for maximizing the charge sensitivity of the PVDF unimorph for given sensor dimensions and deflection sensitivity is provided in section 2. That section also describes the design rationale and fabrication aspects of the cantilever PVDF sensor. The development of a compensated charge amplifier to condition the charge-to-voltage conversion with minimal drift noise for near-static measurements is described in section 3. Characterization experiments aimed at evaluating the performance of a PVDF sensor with the proposed signal conditioner are presented in section 5. That section also describes the problem of pyroelectricity and a simple compensation algorithm that improves the resolution of the pressure sensor.

2. Design and fabrication of piezoelectric cantilever sensor

2.1. Charge sensitivity of cantilever unimorph

Consider a piezoelectric PVDF unimorph beam as shown in figure 1. The overall length and width of the structure are l_S and b_S, respectively. The thicknesses of the PVDF layer and

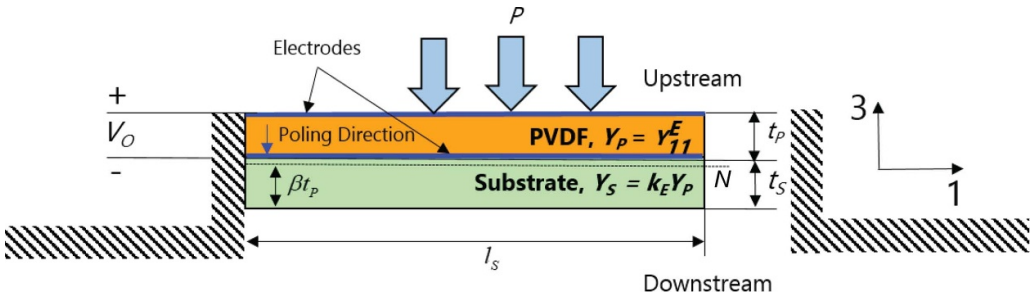

Figure 1. Schematic of a piezoelectric unimorph cantilever sensor subjected to uniform pressure: thicknesses of the PVDF layer and the substrate are t_P and t_S, respectively, and elastic moduli for the PVDF layer under constant electric field and the substrate along direction 1 are Y_P and Y_S, respectively. The length and width of the unimorph are l_S and b_S, respectively. The neutral axis of the structure N is located at βt_P from the bottom of the substrate.

the substrate are t_P and t_S, respectively. The elastic modulus in direction 1 for the PVDF layer under constant electric field is $Y_{11}^E = Y_P$ and the elastic modulus of the substrate is Y_S. The thickness ratio of the structure is defined as $k_t = t_S/t_P$ and the elastic modulus ratio of the structure is defined as $k_E = Y_S/Y_P$. The piezoelectric material is placed on the substrate such that the polarization due to bending (31 mode) deformation is in the same direction as the dielectric polarization. It is assumed that the charge generated by the piezoelectric layer is predominantly due to longitudinal stress T_1 and that the contribution of lateral stress T_2 to the charge output can be neglected due to its smaller magnitude and also due to the d_{32} coefficient being smaller than the d_{31} coefficient [34]. Based on classical laminate theory, it is further assumed that any line perpendicular to the neutral axis before deformation remains perpendicular after deformation, resulting in a strain that varies linearly through the thickness of the beam [35]. For a piezoelectric PVDF film under plane strain conditions, the normal strain in direction 3 and the shear strains 1–3 and 2–3 are assumed to be zero. Using the above approximations, the piezoelectric constitutive equations under quasi-static conditions are reduced to

$$S_{1p}(x,z) = s_{11}^E T_{1p}(x,z) + d_{31} E_3(x,z), \tag{1}$$

$$D_3(x,z) = d_{31} T_{1p}(x,z) + \epsilon_{33} E_3(x,z), \tag{2}$$

where S_{1p} and T_{1p} are the strain and stress, respectively, in the piezoelectric layer; E_3 and D_3 are the electric field and polarization along direction 3; s_{11}^E corresponds to the zero-field compliance of PVDF along direction 1 and is given by the inverse of its elastic modulus; d_{31} is the piezoelectric charge coefficient; and ϵ_{33}^T is the zero-stress dielectric constant of PVDF at constant stress. The distance from the bottom of the substrate to the neutral axis βt_P is represented by

$$z_N = \beta t_P = -\frac{1}{2}\left\{\frac{k_t^2 k_E + 2k_t(1-k_{31}^2) + (1-k_{31}^2)}{k_t k_E + (1-k_{31}^2)}\right\}, \tag{3}$$

where k_{31} is the electromechanical coupling factor of the piezoelectric layer. The effect of elastic modulus of the substrate Y_S on βt_P is significant for compliant substrates and βt_P approaches the value of $-0.5 t_S$ with increasing elastic modulus or thickness of the substrate. For PVDF, the value of k_{31} could be as large as 0.2 [34]. Using strain-displacement relations for the piezoelectric layer and the substrate from Euler–Bernoulli theory, the bending moment about the neutral axis of the unimorph is given by [20]

$$M(x) = \overline{YI}\frac{\partial^2 w(x)}{\partial x^2}, \tag{4}$$

where

$$\overline{YI} = \frac{Y_P b_S t_P^3}{3}\left\{k_E k_t\left(k_t^2 + 3\beta k_t + 3\beta^2\right) + \frac{1}{1-k_{31}^2}\left[\left(1 - \frac{3k_{31}^2}{4}\right) + 3\left(1-k_{31}^2\right)\left(k_t^2 + \beta^2 + 2\beta k_t + k_t + \beta\right)\right]\right\}$$

is the bending stiffness of the piezoelectric unimorph.

The generalized displacement $w(x)$ of the piezoelectric unimorph along the length of the beam is related to the applied pressure $P(x)$ as

$$\overline{YI}\frac{\partial^4 w(x)}{\partial x^4} = b_S P(x). \tag{5}$$

Integrating the above equation, one obtains

$$w(x) = \frac{b_S P(x)}{24\overline{YI}}x^4 + \frac{c_1}{6}x^3 + \frac{c_2}{3}x^2 + c_3 x + c_4. \tag{6}$$

The stresses in the piezoelectric layer and the substrate are given by

$$T_{1p} = -t_P Y_P \frac{\partial^2 w}{\partial x^2} - Y_P d_{31} E_3, \tag{7}$$

$$T_{1s} = -t_S Y_S \frac{\partial^2 w}{\partial x^2}. \tag{8}$$

Using (6) and (7) in (2) and neglecting piezoelectric coupling, $E_3 = 0$, one obtains

$$D_3(x,z) = -d_{31} Y_P t_P (0.5 + k_t + \beta)\frac{\partial^2 w(x)}{\partial x^2}. \tag{9}$$

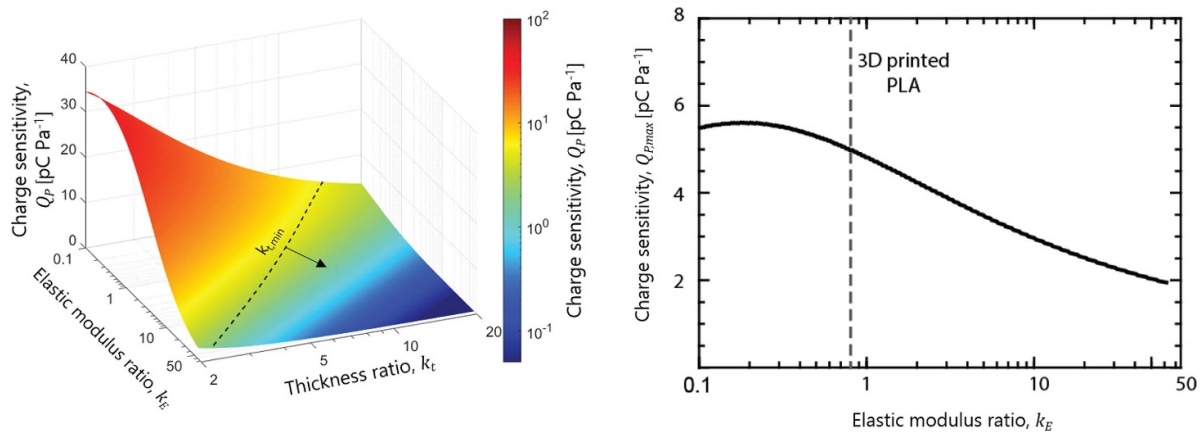

Figure 2. (a) Calculated charge sensitivity Q_P as a function of thickness ratio k_t and elastic modulus ratio k_E. The dashed line indicates the minimum thickness ratio $k_{t,\min}$ for different k_E values. The arrow indicates the feasible region of the substrate design that meets the deflection sensitivity target $\delta_P = 0.5\ \mu\text{m Pa}^{-1}$. (b) Calculated charge sensitivity Q_P along the $k_{t,\min}$ line for different k_E values. The dashed line indicates the k_E value of 3D printed PLA relative to PVDF.

It can be observed that the polarization is proportional to the average stress along the length of the beam. The total charge output of the piezoelectric layer with electrode covered along the length l_S of the unimorph is given by integrating (6) over the surface area A of the electrode as

$$Q = -d_{31} b_S Y_P t_P (0.5 + k_t + \beta) \left[\frac{\partial w(x)}{\partial x}\right]_0^{l_S}. \tag{10}$$

For a cantilever unimorph, using Dirichlet boundary conditions, the boundary conditions at the clamped and free ends can be set as $w(0) = 0$, $w'(0) = 0$, $w''(l) = 0$, $w'''(l) = 0$ in (5) to obtain

$$w(x) = \frac{b_S x^2 (6l_S^2 - 4l_S x + x^2)}{24\overline{YI}} P. \tag{11}$$

Thus, the deflection sensitivity δ_P of the unimorph is given by the maximum displacement per unit applied pressure as

$$\delta_P = \frac{w_{\max}}{P} = \frac{b_S l_S^4}{8\overline{YI}}. \tag{12}$$

Finally, the charge sensitivity of the cantilever unimorph is obtained using (11) in (10) as

$$Q_P = \frac{Q}{P} = -\frac{0.167 d_{31} b_S^2 Y_P t_P l_S^3}{\overline{YI}} (0.5 + k_t + \beta). \tag{13}$$

2.2. Design optimization procedure

The thickness ratio k_t and the elastic modulus ratio k_E are investigated over the ranges from 2 to 20 and from 0.1 to 70, respectively. Figure 2(a) shows the calculated charge sensitivity Q_P as a function of thickness ratio k_t and elastic modulus ratio k_E using the geometric and material properties provided in table 1. In order to meet a maximum overall thickness target of 1 mm and maximum pressure input target of 2 kPa, the deflection sensitivity δ_P (defined as deflection per unit applied pressure) is limited to $0.5\ \mu\text{m Pa}^{-1}$. For a given k_E, the minimum thickness ratio k_t which meets the target δ_P is represented by the dashed line $k_{t,\min}$ in figure 2(a). It can be observed that the maximum charge sensitivity $Q_{P,\max}$ in the feasible region (represented by the arrow) occurs along $k_{t,\min}$. Figure 2(b) shows $Q_{P,\max}$ along the $k_{t,\min}$ line for different k_E values.

The optimal elastic modulus ratio k_E for maximum charge sensitivity along $k_{t,\min}$ is calculated to be 0.2. In order to facilitate rapid prototyping of the sensor using a commercial 3D printer, polylactic acid (PLA) polymer is chosen as the closest material to optimal for the substrate. The elastic modulus ratio k_E of the 3D printed PLA relative to PVDF is specified as 0.73 (i.e., $Y_S/Y_P = 2\ \text{GPa}/2.74\ \text{GPa}$) [36]. The minimum thickness ratio k_t corresponding to the elastic modulus ratio k_E is 7 (i.e., $t_S/t_P = 0.198\ \text{mm}/0.028\ \text{mm}$). The charge sensitivity of the cantilever unimorph subjected to uniform pressure loading is thus calculated to be $5.05\ \text{pC Pa}^{-1}$. This value is slightly lower than the maximum achievable charge sensitivity of $5.60\ \text{pC Pa}^{-1}$ along $k_{t,\min}$, but it allows for easier fabrication.

2.3. Fabrication

The sensor frame and the cantilever substrate is printed as a monolith using a commercial fused deposition modeling (FDM) printer (Ultimaker S5). Polylactic acid (PLA, Ultimaker) is printed at 190 °C with 100% infill diagonal raster, at a rate of 25 mm s^{-1}. The layer resolution of the 3D printer is set at 40 μm. The schematic of the sensor is shown in figure 3(a). A commercial 28 μm thick PVDF film (Measurement Specialties) with sputtered silver electrodes is precisely cut to a 17.0 mm length and 10.5 mm width. The edges (about 0.2 mm) on the cantilever arm side are etched away with acetone to prevent a short circuit. Copper tapes with conductive adhesive (3M 1181 EMI shielding copper

Table 1. Geometric and material properties of the fabricated cantilever PVDF pressure sensor.

Geometric parameters of the sensor		Material properties of the PVDF film	
Length × width of the cantilever $l_S \times b_S$	10×10 (mm^2)	Elastic modulus of PVDF film, Y_P	2.74 (GPa)
Thickness of the PLA, t_S	0.196 (mm)	Relative permittivity of PVDF, ε_r	11–13
Thickness of PVDF film, t_P	28 (μm)	Piezoelectric charge coefficient of PVDF film in direction 1, d_{31}	24 (pC N^{-1})
Overall length of the sensor	22 (mm)	Piezoelectric charge coefficient of PVDF film in direction 2, d_{32}	3 (pC N^{-1})
Overall width of the sensor	14 (mm)	Piezoelectric charge coefficient of PVDF film in direction 3, d_{33}	-34 (pC N^{-1})
Overall thickness of the sensor	1.3 (mm)	Pyroelectric coefficient of PVDF film, p	30 (μC m^{-2}°C^{-1})

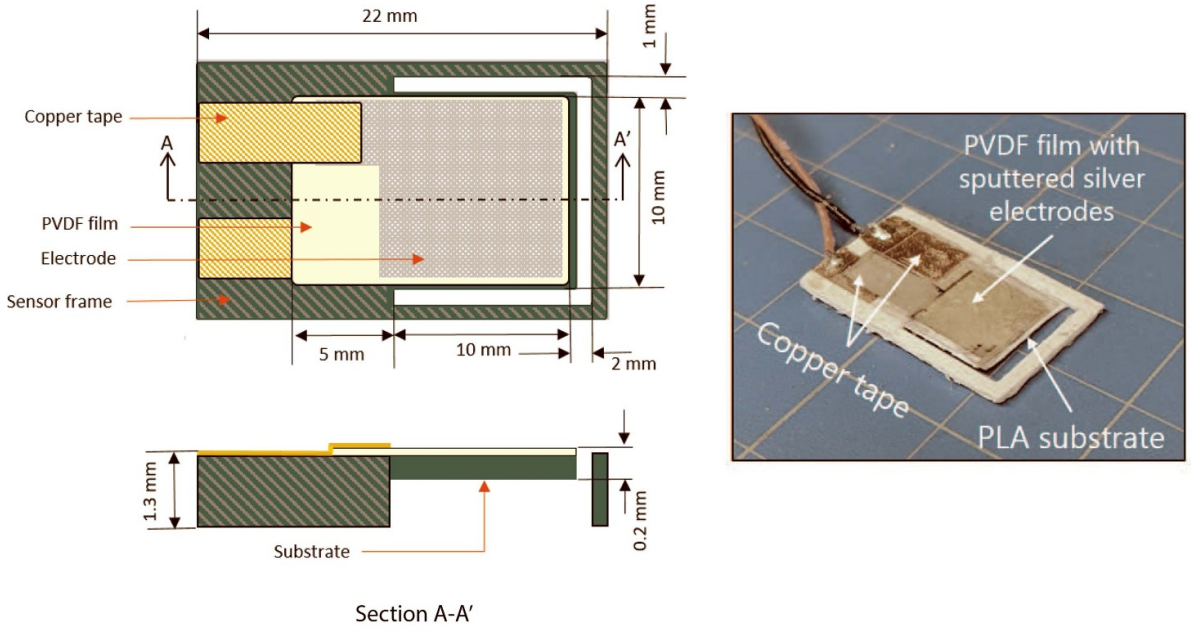

Figure 3. (a) Schematic and dimensions of the cantilever unimorph. (b) Photograph of the fabricated cantilever unimorph.

tape, 70 μm thick) that are 10 mm long and 3 mm wide are attached to both sides of the PVDF film. A thin acrylic coat (Rust-oleum) is sprayed onto the film on both sides to provide structural integrity between the PVDF film and the copper tape and dried at room temperature for 24 h. The PVDF film with copper tape is then attached onto the sensor frame and cantilever arm of the 3D printed part using a thin layer of cyanoacrylate glue (3M SI100) and clamped for 30 min. Finally, the leads are soldered to the copper tape as shown in figure 3(b). The capacitance of the fabricated sensor is measured using a digital multimeter (Fluke 175) to be 0.65 nF.

3. Signal conditioner for near static measurements

Charge amplifiers are transcapacitance circuits that process electric charge into measurable voltage by integration [37]. A basic charge amplifier can be realized using discrete electronic components designed with an operational amplifier and an $R_F C_F$ feedback network. The piezoelectric sensor is modeled as a capacitor C_S with a finitely large output impedance R_S connected in parallel to a charge output Q_S. The frequency characteristics of the charge amplifier are typically those of a band-pass filter with its lower cutoff frequency determined by the sensor impedance Z_S and the feedback impedance Z_F. The upper cutoff frequency is determined by the impedance Z_I comprised of a low pass resistor R_I, sensor capacitance C_S, and the open loop gain A_{OL} of the operational amplifier. A detailed analysis of the effect of the sensor and feedback impedances on the sensitivity and passband frequency of a basic charge amplifier is provided in [12]. In order to facilitate static measurement, the feedback resistance $R_F \to \infty$, such that the lower cutoff frequency $f_{LC} \to 0$. Therefore, a practical implementation of a high feedback resistance is to utilize polypropylene type capacitors which offer high insulation resistance on the order of TΩ. If $C_S \leqslant C_F$, the voltage gain or the calibration factor of the charge amplifier S_Q can be approximated to $1/C_F$.

The main drawback of a large-timeconstant charge amplifier is its sensitivity to input bias currents I_{B-} and I_{B+},

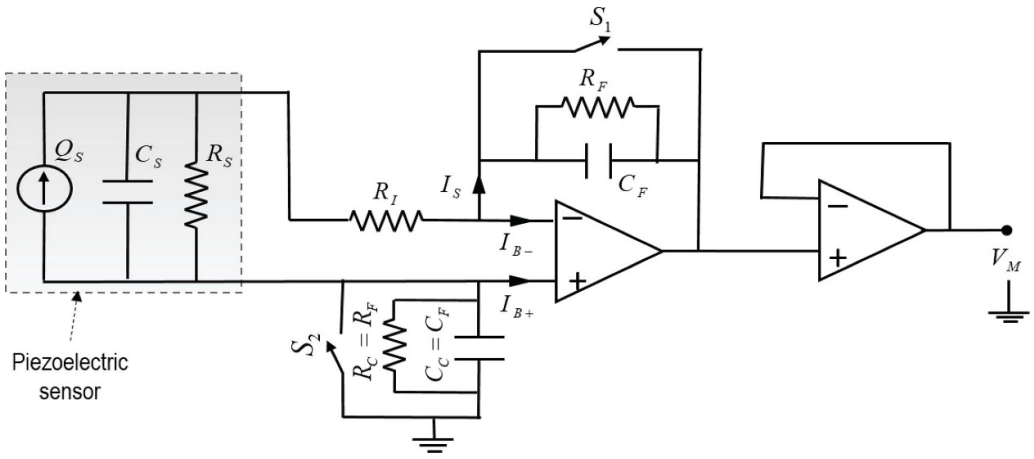

Figure 4. Schematic of the signal conditioner utilized in this work.

resulting in a drifting output voltage which contributes to measurement noise and also eventually drives the op-amp into saturation. Therefore, almost all low frequency applications involving charge amplifiers employ a finite feedback resistance on the order of MΩ to provide a dc path for the input bias current, thereby simultaneously reducing the overall time constant of the system [13, 24, 38]. The input bias currents for commercial operational amplifiers range from several nA to fA. The input bias currents also exhibit a direct relationship with temperature. For a charge amplifier with a smaller time constant, the effect of input bias currents is negligible. However, as the time constant is increased, the accumulated error over time becomes larger than the resolution of the pressure sensor. This inhibits direct measurement using a charge amplifier for static measurements. The drifting voltage also limits the operational time of the charge amplifier due to saturation. The voltage drift rate e_d can be decreased by using a low bias current operational amplifier or reducing the voltage gain S_Q. Therefore, in order to maximize the resolution of the pressure sensor over large measurement periods for a given bias current, the charge sensitivity Q_P must be maximized. This requirement could be achieved by increasing the area of the sensor A_S, but this also increases its capacitance and pyroelectric sensitivity. Thus, there is a need to develop an effective compensation design to reduce e_d while simultaneously increasing S_Q.

Several techniques have been utilized for automated drift compensation in the literature. We recently proposed an automated drift compensation topology for near-static measurements using piezoelectric films [12]. A drawback of that topology is that the operational time is limited by saturation of the operational amplifier. In order to overcome these limitations, a compact version of the differential topology for automated drift compensation is utilized in this work. The topology is obtained by adding another impedance equal to the feedback impedance $R_C C_C$ to the common single-ended charge amplifier instead of utilizing another op-amp to compensate for drift voltage. The impedance is placed between the op-amp's non-inverting input and ground, as shown in figure 4. The charge amplification stage is followed by a unity gain buffer circuit to provide a low impedance interface to the data acquisition device. The output voltage $V_M(s)$ for a step charge input to the compensated charge amplifier is given by

$$V_M(s) = \left(\frac{S_{Qf}}{s+f_{lf}} + \frac{S_{Qc}}{s+f_{lc}}\right) sQ(s) + \left(\frac{S_{Qf} I_{B-}}{s+f_{lf}} - \frac{S_{Qc} I_{B+}}{s+f_{lc}}\right), \tag{14}$$

where the subscript f corresponds to the feedback part of the circuit and the subscript c corresponds to the compensating part of the circuit. Assuming $C_F = C_C$, $C_S \ll C_F$, and $R_F = R_C$, (14) is reduced to

$$V_M(s) = \left(\frac{2S_{Qf}}{s+f_{lf}}\right) sQ(s) + \left\{\frac{S_{Qf} I_{B-}}{s+f_{lf}} (1-\alpha_B)\right\}, \tag{15}$$

where $\alpha_B = I_{B+}/I_{B-}$. Due to the differential configuration, the passband gain S_Q of the charge amplifier is twice that of the basic single-ended configuration. As the cutoff frequency $f_{lf} \to 0$, the variations in the component tolerances of the capacitances C_F and input bias currents I_{B-} and I_{B+} manifest as error in long time static measurements. Therefore, perfectly matched capacitors C_F and C_C (with leakage resistance $R_F > 1$ TΩ) and operational amplifiers with low bias currents (<0.1 pA) and high open loop gain (>100 dB) are required to minimize drift rate.

The compensated charge amplifier is implemented using a low offset, ultra low bias current CMOS operational amplifier LMC6082 (Texas instruments) with a chosen feedback capacitance $C_{FA} = 10.14$ nF and compensating capacitance $C_{CA} = 10.16$ nF. The open-loop voltage gain of the operational amplifier is $A_{OL} = 130$ dB and the input resistance R_I is chosen as 1 MΩ. The upper cutoff frequency of the charge amplifier is thus calculated to be 2.47 kHz. Normally-open switches placed across the feedback and compensating capacitors are actuated simultaneously prior to the start of the measurement to reset the circuit by draining any stored charge. The operational amplifier is powered by three 1.5 V batteries. Polypropylene feedback capacitors are chosen for their high leakage resistance values on the order of TΩ. The sensitivity of the charge amplifier for the active sensor is calculated to be

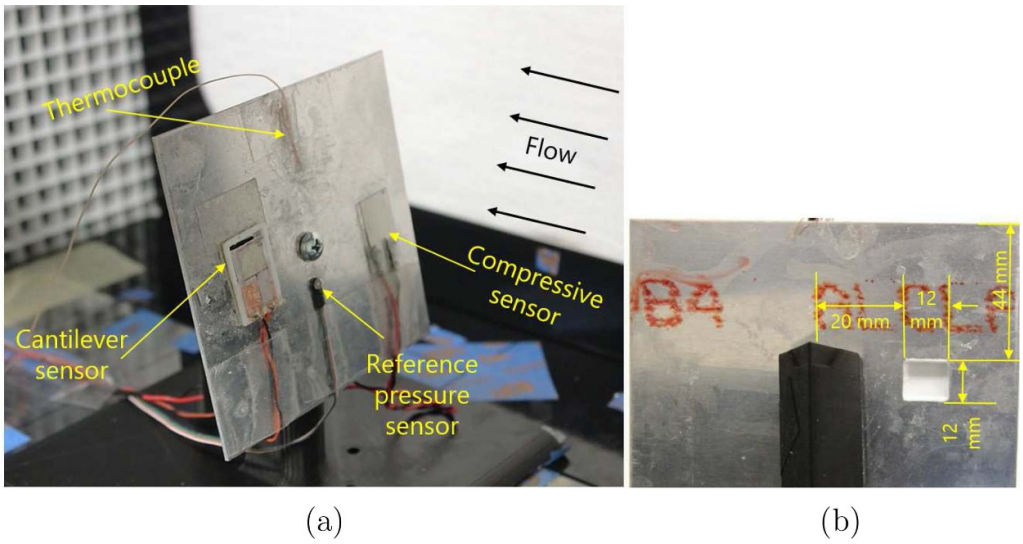

Figure 5. (a) Experimental setup inside the wind tunnel for characterizing the PVDF pressure sensor. The pressure measurement panel is a flat plate with a square cutout that accommodates the cantilever PVDF sensor. The compensating PVDF sensor in compressive mode is positioned symmetrically on the other half of the flat plate. The applied pressure and temperature are monitored using a reference piezoresistive pressure sensor and thermocouple, respectively. (b) Machined cutout shown from the back side of the pressure measurement panel.

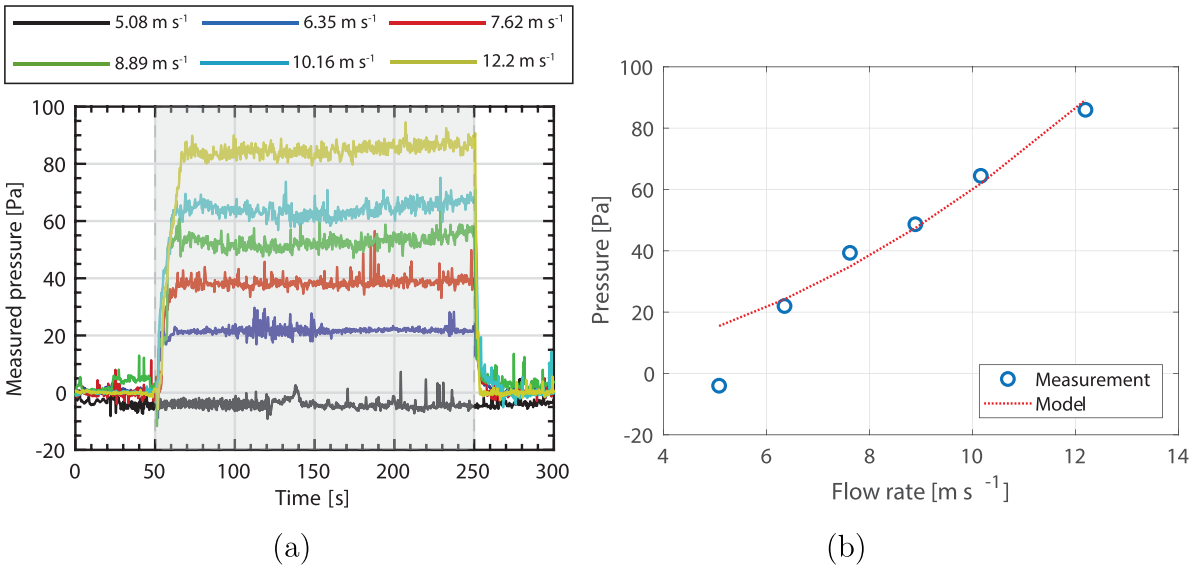

Figure 6. (a) Measured reference pressure P at different flow rates. The shaded region indicates the time window when the flow is ON. (b) Average pressure measured using the reference pressure sensor at different flow rates compared against $P = \frac{1}{2}C_D\rho U^2$.

0.19 mV pC^{-1}. The uncompensated single-ended charge amplifier accumulates error of 0.25 mV over a minute, whereas the compensated charge amplifier accumulates less than 0.05 mV over the same time period. The theoretical pressure sensitivity $K_{Q,cant}$ of the active cantilever sensor interfaced with the compensated charge amplifier is thus calculated to be 0.99 mV Pa^{-1}.

4. Pyroelectric effect in wind tunnel measurements

The pyroelectric response is a consequence of the polarization temperature dependence, which leads to the appearance of uncompensated electric charge at the crystallographic surface. The pyroelectric characteristics of PVDF sensors are well established in the literature [39, 40]. Due to the non-uniform temperature field in a wind tunnel environment, it is difficult to experimentally characterize the differential pressure sensor under constant temperature. Unlike typical force or strain inputs, an aerodynamic pressure input is almost always accompanied by a thermal component. Piezoelectric sensors measure changes from an initial state. Conventional stress measurements are carried out in a varying environment after stabilization of ambient temperature [13]. Such a stabilization phase is not possible in a wind tunnel environment. Neglecting

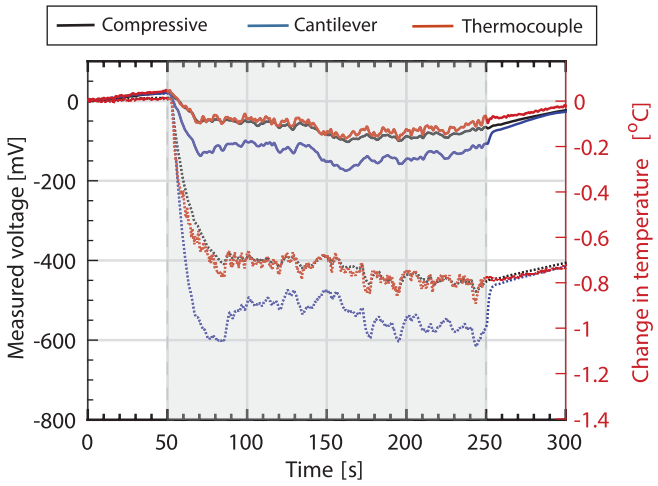

Figure 7. Responses of the cantilever and compressive PVDF sensors interfaced with the compensated charge amplifier and compared against the thermocouple measurements. The solid lines and dotted lines indicate measurements at low pressure ($P = 23$ Pa) and high pressure ($P = 85$ Pa), respectively. The initial temperature is 26.8 °C.

temperature induced stress, the net charge displacement of a piezoelectric sensor is the algebraic sum of the piezoelectric and pyroelectric effects,

$$D_3(t,T) = \underbrace{d_{ij}(T)T_j}_{\text{piezoelectric}} + \underbrace{p(T)\,\Delta T(t)}_{\text{pyroelectric}}, \tag{16}$$

where T is the average temperature, p is the pyroelectric coefficient, and ΔT is the change in average temperature of the piezoelectric material. For PVDF, the pyroelectric coefficient at 25 °C is specified to be $p = 30\,\mu\text{C m}^{-2}\,^{\circ}\text{C}^{-1}$ [34]. The transfer function relating voltage and change in temperature under constant mechanical stress is calculated from (15) as

$$\left|\frac{V_M(s,T)}{\Delta T(s)}\right|_{T_j} = \frac{sp(T)A_S S_Q}{s + f_{LCF}}. \tag{17}$$

Many piezoelectric sensor applications compensate for the change in piezoelectric sensitivity due to changes in temperature [30, 41], but applications that compensate for the transient pyroelectric effect are limited. This is due to the fact that voltage due to pyroelectricity is generally not significant in an environment where the rate of change of temperature $s\Delta T(s) \ll f_{\text{LCF}}$. However, when the sensor system has an extremely low cutoff frequency in order to handle near-static measurements, the pyroelectric sensitivity of the PVDF sensor becomes significant. For the PVDF sensor utilized in this work, the pyroelectric voltage sensitivity at 25 °C is calculated to be $pA_S S_Q = 570\,\text{mV}\,^{\circ}\text{C}^{-1}$. In order to isolate the piezoelectric component from the total voltage response, a simultaneous measurement of temperature becomes mandatory. The pyroelectric compensator for the active sensor should have the following characteristics: accurate measurement of change in temperature; minimal sensitivity to the applied pressure; minimal footprint; simple signal processing; and minimal noise.

In this regard, an additional PVDF sensor of the same pyroelectric sensitivity (pyroelectric coefficient p and sensing area A_S) in compressive mode is introduced. The theoretical pressure sensitivity of the compressive mode sensor $K_{Q,\text{comp}}$ is nearly three orders of magnitude lower than that of the active cantilever sensor ($d_{33}A_S S_Q = 0.66\,\mu\text{V Pa}^{-1}$). Therefore, within the investigated pressure range, the voltage response of the compressive sensor can be assumed to be only due to pyroelectricity. The advantage of this compensation technique is the possibility of integrating the pyroelectric compensator in the cantilever PVDF sensor, such that both sensors exhibit the same transient characteristics. The signal conditioner can also be constructed on a quad operational amplifier with two amplifiers dedicated for the active sensor and the other two amplifiers for the compensator. Such a construction will provide compactness and minimal error.

5. Experiments

5.1. Experimental setup

A wind tunnel (X-Stream, Pitsco) is used to experimentally characterize the performance of the piezoelectric differential pressure sensor under different pressures. The wind tunnel has a flow straightener with a 6:1 compression ratio intake bell to laminarize the flow. The test chamber of the wind tunnel is $500 \times 300 \times 300$ mm. It is equipped with a handheld control to adjust the wind speed up to 15 m s^{-1} and a manometer to monitor the flow velocity.

The pressure measurement panel is a 100×100 mm flat plate with a 12×12 mm square cutout for mounting the piezoelectric cantilever sensor. The panel is mounted on a 3D-printed platform. The fabricated cantilever sensor shown in figure 3 is attached at the square slot using double-sided tape. A commercial pressure sensor (LQ-062, Kulite) with a 0–35 kPa range and a full scale output of 100 mV is utilized for monitoring the applied pressure [42]. A 10×10 mm PVDF sensor is used in compressive mode and attached symmetrically on the other half of the flat plate using cyanoacrylate glue as shown in figure 5. The temperature change due to the airflow is monitored with an AWG40 thermocouple (Omega Engineering). The measurements are recorded using a data acquisition system (NI 9239, National Instruments) at a sampling rate of 10 Hz.

The experimental characterization of the fabricated piezoelectric sensor is conducted with the wind tunnel turned off for 50 s and then turned on for the next 200 s. The applied differential pressure is monitored using the reference pressure sensor and the flow rate is monitored using a manometer connected to the wind tunnel. Due to the low sensitivity of the piezoresistive sensor, the measured signal is smoothened using the Gaussian method (50 points) after removing the residual unbalance present before each test. It is assumed that the applied pressure is symmetric laterally across the panel surface [43]. The flow is turned off immediately after 200 s and the data is collected while the temperature goes back to equilibrium for another

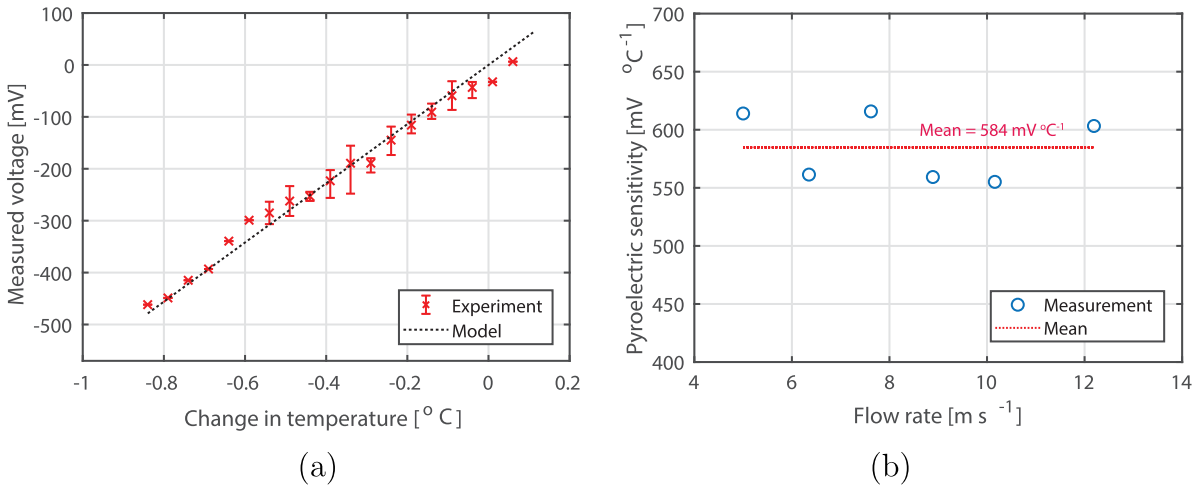

Figure 8. (a) Measured voltage of the compressive mode PVDF sensor versus change in temperature when the flow is ON compared against the voltage predicted by the model, $V_D = pA_S S_Q \Delta T$. The error bars indicate the variation in the measured voltage for a given change in temperature. (b) Measured pyroelectric sensitivity for different input flow rates.

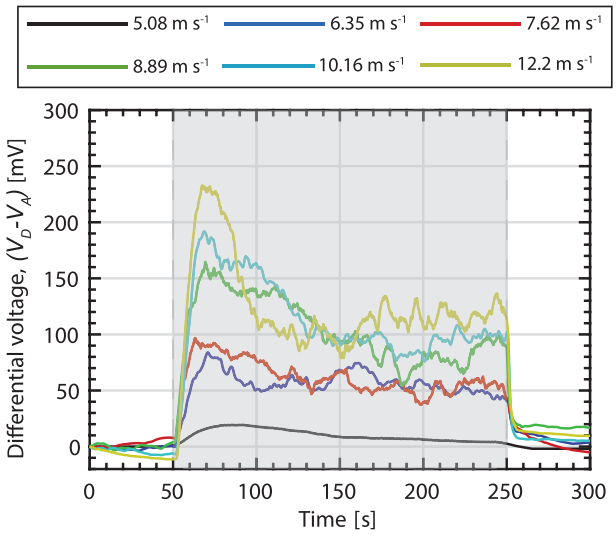

Figure 9. Measured differential voltage ($V_D - V_A$) at different input flow rates.

50 s. The next measurement is taken after resetting the charge amplifier circuit to zero.

5.2. Experimental results

Figure 6(a) shows the smoothened pressure values measured by the commercial pressure sensor at different flow rates. The pressure sensor has poor response at low flow rates due to its sensitivity. However, at higher flow rates, the smoothened response of the commercial sensor is found to be sufficient to monitor the applied pressure. Assuming laminar flow and incompressibility, the input flow velocity U is related to the applied differential pressure P as $\frac{1}{2}C_D\rho U^2$ where $C_D = 1.051$ is the drag coefficient of a flat plate at an angle of 80° [43] and ρ is the density of air at 25 °C. For flow rates $U > 6\,\mathrm{m\,s^{-1}}$, figure 6(b) indicates that the averaged reference pressures are in good agreement with the flow rates measured by the manometer. These pressure values serve as references against which the piezoelectric sensor is calibrated.

Figure 7 shows the response of the cantilever and compressive PVDF sensors interfaced with the compensated charge amplifier at two different pressures. The drops in temperature during the wind tunnel measurements were measured to be as high as 0.8 °C. The secondary y-axis indicates the change in temperature measured by the thermocouple and is scaled based on the pyroelectric sensitivity value calculated in the previous section. Together, the plots demonstrate the static measurement capability of the signal conditioner. No significant phase difference is observed between the thermocouple and compressive PVDF sensor for either pressure condition. When the flow is turned on, the cantilever sensor responds to both pressure and thermal inputs, whereas the compressive sensor responds primarily to temperature. Further, it can be observed that the average difference between the cantilever and the compressive sensor voltages increases with the increase in the applied pressure P. Once the flow is turned off, the cantilever sensor voltage (V_A) immediately drops to the level of the compressive sensor voltage (V_D), indicating that the differential voltage $|V_A - V_D|$ is due to the piezoelectric component of the signal.

Figure 8(a) shows the relationship between the compressive sensor voltage with respect to change in temperature at different pressures. Within the investigated range, the sensor exhibits good repeatability and a linearity of 99% with respect to the thermocouple, thus validating the assumption of its negligible pressure sensitivity. A compressive-mode sensor could serve as an excellent alternative to thermocouples for high-resolution, low-temperature measurements. The sensitivity measured from the linear fit of figure 8(a) is $530\,\mathrm{mV\,°C^{-1}}$ which is within 7% of the pyroelectric sensitivity of $570\,\mathrm{mV\,°C^{-1}}$ calculated in section 5. Figure 8(b) shows the pyroelectric sensitivities calculated at different flow rates. Within the investigated range, no direct relationship is observed between the measured pyroelectric sensitivity and flow rate. The standard deviation in the average sensitivity at

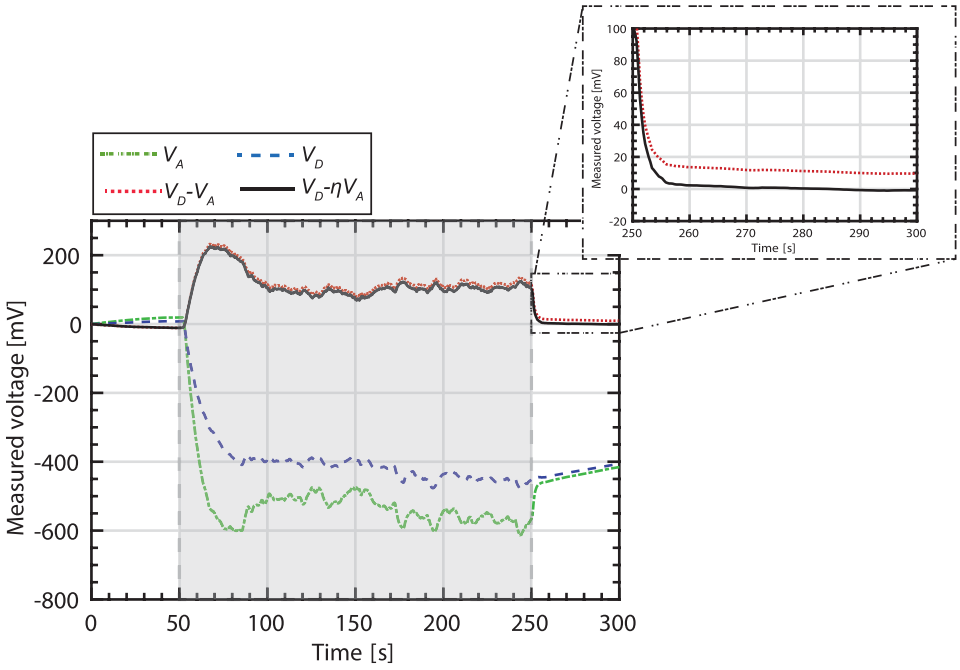

Figure 10. Comparison of differential voltage responses from the cantilever PVDF sensor with and without the pyroelectric compensation algorithm. This plot is for the case $P = 85$ Pa.

different flow rates is calculated to be 27 mV °C^{-1}, which is within 5% of the mean pyroelectric sensitivity. The average pyroelectric sensitivity computed from figure 8(b) is 584 mV °C^{-1}, which is 2.5% greater than the model result.

5.3. Pyroelectric compensation algorithm

PVDF sensor devices can exhibit profound variation in their pyroelectric responses owing to a number of extrinsic factors other than the pyroelectric coefficient p and sensing area A_S, such as the geometric and material parameters of the substrate, the heat transfer coefficient between the sensor, substrate, and environment, and the initial temperature [39]. Due to this variation, pyroelectric response modeling in the time domain is largely developed using data-driven approaches [31, 44]. Figure 9 shows the differential voltage measured at different flow rates. A positive correlation between flow rate and differential voltage is observed. The differential voltage exhibits faster response to the applied pressure as observed when the pressure is turned on or off. However, stability in the compensated response is not achieved until about a minute after the flow is turned on. This is due to the smaller thermal time constant (faster response) of the cantilever sensor compared with the compressive sensor, which is primarily a result of differences in heat transfer coefficients and temperature variation as a result of the airflow. This difference in transient thermal characteristics is observed as large variations in the differential voltages in figure 9. Further, it can be seen that the residual offset due to different thermal characteristics could be as high as 25 mV after the flow is turned off. Therefore, a simple empirical approach is adopted to adjust the pyroelectric sensitivity of the cantilever sensor to minimize the residual offset and thereby improve the resolution of the pressure sensor.

The algorithm involves adjusting the gain of the cantilever sensor by a correction factor η, such that when the air flow is turned off (250–300 s) the difference between the cantilever and the compressive sensor voltages is minimal. The gain is adjusted for each run and the correction factor is recalculated to minimize residual error after the flow is turned off. The next measurement is taken after the differential voltage is free of any residual thermal drift. The different components of the compensation algorithm are shown in figure 10. The correction factor η is estimated such that

$$\eta = \arg\min \sum_{t=250}^{t=300} \left[V_D(t) - \eta V_A(t)\right]^2. \tag{18}$$

The above regression model uses a trust-region reflective least squares method, which allows for estimation of the correction factor η driving the model. The corrected compensating voltage $\eta V_A(t)$ is then subtracted from the response of the compressive sensor to obtain its response due to pressure input only, as shown in figure 10. As observed in figure 8(b) in the pyroelectric performance of the compressive sensor, no direct relationship is observed between the applied pressure P and correction factor η.

The temperature compensation algorithm is applied to the measured voltage of the cantilever sensor for each test, yielding the compensated voltage responses shown in figure 11(a). Once the compensated voltage reaches steady state, the sensor is able to resolve the static differential pressure up to 10 Pa. Figure 11(b) demonstrates the linearity of the cantilever pressure sensor. The mean voltage computed in the stabilized region (150–250 s) exhibits good linearity of 97.3% with respect to the reference pressure sensor in the same region. The sensitivity of the sensor thus obtained by linear regression

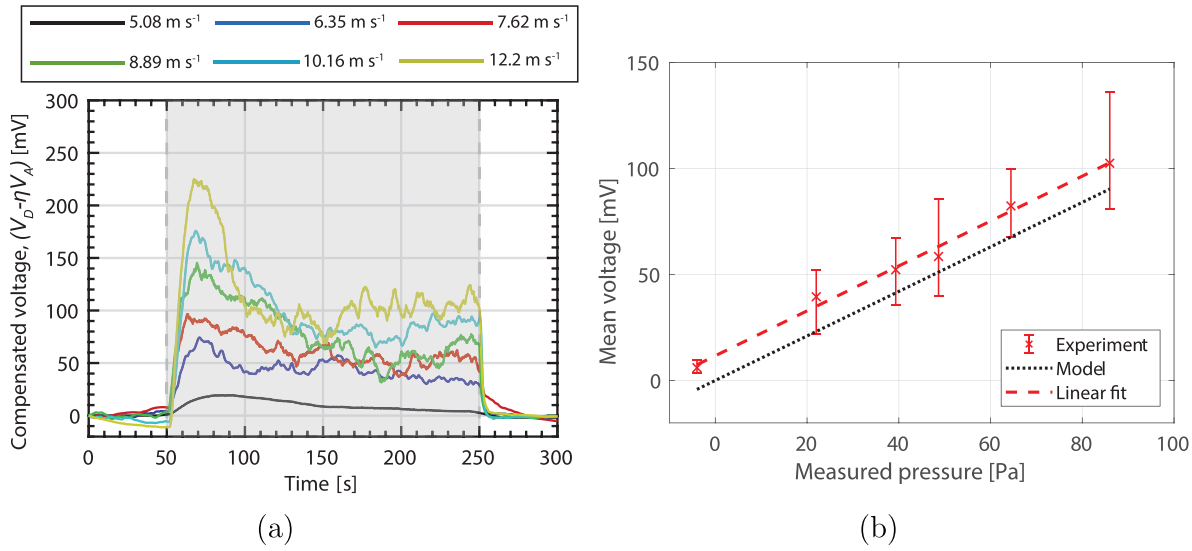

Figure 11. (a) Compensated voltages ($V_D - \eta V_A$) of the cantilever pressure sensor at different differential pressures. (b) Average compensated voltage (dashed red line) versus measured pressure (red markers) compared against the theoretical sensitivity (dotted black line).

of the corresponding data points is 1.05 mV Pa^{-1}. The theoretical (model) sensitivity is calculated using (13) and (14) to be 0.99 mV Pa^{-1}. The measured sensitivity is slightly higher by 5.7%, primarily due to the presence of residual pyroelectric voltage in the compensated sensor voltage.

6. Concluding remarks

This work demonstrates near-static differential pressure sensing with a cantilever PVDF unimorph by interfacing it with a novel compensated charge amplifier design. A generalized expression for deflection and polarization of piezoelectric bending unimorphs is developed in order to model deflection and charge sensitivities for the PVDF cantilever unimorph under uniform pressure loading. An analytical design framework is presented for maximizing the charge sensitivity of the sensor while meeting the deflection sensitivity target of 0.5 μm Pa^{-1}. The conflicting requirements of maximizing the time constant and minimizing the voltage drift of a basic charge amplifier for near-static measurements is addressed by designing and implementing a drift compensation circuit using commercially available components. The fabricated sensor is experimentally characterized from 0 to 80 Pa input pressure using a laboratory wind tunnel. The pyroelectric response is compensated by incorporating a compressive-mode pressure sensor interfaced with a similar compensated charge amplifier. The advantage of the proposed compensation technique is that noise is minimized in the compensated voltage output because the pressure and compensation sensors utilize the same piezoelectric measurement principle, unlike thermocouple-based compensation techniques. Also, there is a possibility of packaging the compensator within the cantilever structure through micro-fabrication. Owing to different thermal time constants, airflow rate, and effect of initial temperature on the decay response of the cantilever and compressive sensors, the gain of the cantilever sensor is adjusted by a calibration factor. The sensor has a measured sensitivity of 1.05 mV Pa^{-1}, exhibits good linearity of 97.3% with respect to the mean reference pressure, and has an average resolution of 10 Pa. The measured sensitivity closely matches the theoretical sensitivity, having an error of $<$5.7% within the investigated range. The residual error and necessity of a compensation algorithm can be further eliminated through design of a pyroelectric compensator with matched thermal characteristics. This can be achieved by integrating the pyroelectric compensator onto the active sensor itself such that both sensors exhibit the same transient thermal characteristics.

Acknowledgments

Financial support was provided by the member organizations of the Smart Vehicle Concepts Center, a Phase III National Science Foundation Industry-University Cooperative Research Center (www.SmartVehicleCenter.org) under Grant NSF IIP 1738723.

ORCID iDs

Leon M Headings https://orcid.org/0000-0003-1499-140X
Marcelo J Dapino https://orcid.org/0000-0003-4888-1903

References

[1] Yamashita T, Makihara T, Maeda K and Tadakuma K 2017 *SAE Int. J. Passenger Cars-Mech. Syst.* **10** 358–68
[2] Zhu W, Li C, Zhong Y and Lin P 2017 *SAE Int. J. Mate. Manuf.* **10** 107–13
[3] Fiorillo A, Critello C and Pullano S 2018 *Sensors Actuators A* **281** 156–75

[4] Stathopoulos T, Zisis I and Xypnitou E 2014 *J. Wind Eng. Ind. Aerodyn.* **125** 195–206
[5] Gomes M, Rodrigues A and Mendes P 2005 *J. Wind Eng. Ind. Aerodyn.* **93** 741–56
[6] Zagnoni M, Golfarelli A, Callegari S, Talamelli A, Bonora V, Sangiorgi E and Tartagni M 2005 *Sensors Actuators A* **123** 240–48
[7] An L, Lu T, Xu J, Wang Z, Xu M and Wang T 2018 *Int. J. Mech. Sci.* **141** 386–92
[8] Le Sant Y and Merienne M 2005 *Aerosp. Sci. Technol.* **9** 285–99
[9] Bian Y, Liu R, Huang X, Hong J, Huang H and Hui S 2015 *Smart Mater. Struct.* **24** 105001
[10] Sengupta D, Kottapalli A G P, Chen S H, Miao J M, Kwok C Y, Triantafyllou M S, Warkiani M E and Asadnia M 2017 *AIP Adv.* **7** 105205
[11] Mahbub I, Shamsir S, Islam S K, Pullano S A and Fiorillo A S 2017 *2017 IEEE 60th International Midwest Symposium on Circuits and Systems (MWSCAS)* pp 875–8
[12] Ramanathan A K, Headings L M and Dapino M J 2020 *Sensors Actuators A* **301** 111654
[13] Ma Z, Wang G, Rui X, Yang F and Wang Y 2019 *Smart Mater. Struct.* **28** 9
[14] Nitsche W, Mirow P and Szodruch J 1989 *Exp. Fluids* **7** 111–8
[15] Luber W and Becker J 2011 *Structural Dynamics* vol 3 (Berlin: Springer) pp 1157–76
[16] Zhang X, Shan X, Shen Z, Xie T and Miao J 2019 *Sensors* **19** 962
[17] Wang Y, Huang C, Lee Y and Tsai H 2006 *Exp. Fluids* **41** 365–73
[18] Niu M and Kim E 2003 *J. Microelectromech. Syst.* **12** 892–98
[19] Mo C, Davidson J and Clark W 2014 *Smart Mater. Struct.* **23** 045005
[20] Pillai M, Ebenezer D and Deenadayalan E 2017 *J. Acoust. Soc. Am.* **142** 718–27
[21] Ramanathan AK, Headings L M and Dapino MJ 2019 *Proc. SPIE* **10973** p 1097307
[22] Takahashi H, Dung N, Matsumoto K and Shimoyama I 2012 *J. Micromech. Microeng.* **22** 055015
[23] Takahashi H, Isozaki A, Matsumoto K and Shimoyama I 2015 *2015 28th IEEE International Conference on Micro Electro Mechanical Systems (MEMS)* pp 706–9
[24] Tomimatsu Y, Takahashi H, Kobayashi T, Matsumoto K, Shimoyama I, Itoh T and Maeda R 2013 *2013 Joint IEEE Int. Symp. on Applications of Ferroelectric and Workshop on Piezoresponse Force Microscopy (ISAF/PFM)* pp 336–9
[25] Wang Z, Wang C and Liu L 2005 *IEEE Trans. Ultrason. Ferroelectr. Freq. Control* **52** 1840–50
[26] Smits J and Choi W 1991 *IEEE Trans. Ultrason. Ferroelectr. Freq. Control* **38** 256–70
[27] Khan A, Abas Z, Kim H and Oh I 2016 *Smart Mater. Struct.* **25** 053002
[28] Cong J, Jing J and Chen C 2019 *Sensors* **19** 1404
[29] Kim Y, You K and You J 2014 *Sci. World J.* **2014**
[30] Wang D F, Lou X, Bao A, Yang X and Zhao J 2017 *Appl. Phys. Lett.* **111** 083502
[31] Fendzi C, Rebillat M, Mechbal N, Guskov M and Coffignal G 2016 *Struct. Health Monit.* **15** 525–40
[32] Bur A and Roth S 1986 Dynamic polymer pressure transducer with temperature compensation *US Patent* 4 577 510
[33] Ramanathan A K, Headings L M and Dapino M J 2020 *Proc. SPIE* **11382** p 113820I
[34] Measurement Specialties Inc. 1999 *Piezo Film Sensors Technical Manual*
[35] Reddy J 2004 *Mechanics of Laminated Composite Plates and Shells: Theory and Analysis* (Boca Raton: CRC Press)
[36] Lanzotti A, Grasso M, Staiano G and Martorelli M 2015 *Rapid Prototyp. J.* **21** 604–17
[37] Massarotto M, Carlosena A and Lopez-Martin A 2008 *IEEE Trans. Instrum. Meas.* **57** 309–20
[38] Sirohi J and Chopra I 2000 *J. Intell. Mater. Syst. Struct.* **11** 246–57
[39] Eliseev E, Morozovsky N, Yelisieiev M and Morozovska A 2016 *J. Appl. Phys.* **120** 174102
[40] Tzou H and Ye R 1996 *Mech. Syst. Signal Process.* **10** 459–69
[41] Sharma S, Vig R and Kumar N 2016 *J. Intell. Mater. Syst. Struct.* **27** 2524–35
[42] Kulite Semiconductor P 2012 *Kulite Strain Gage Manual*
[43] Ortiz X, Rival D and Wood D 2015 *Energies* **8** 2438–53
[44] Odon A 2010 *Meas. Sci. Rev.* **10** 195–9